Research Square

Preprints are preliminary reports that have not undergone peer review.
They should not be considered conclusive, used to inform clinical practice,
or referenced by the media as validated information.

Internal electric field design suppresses ion migration in perovskite solar cells

Yang Yang

yangy@ucla.edu

University of California, Los Angeles https://orcid.org/0000-0001-8833-7641

Zhichao Shen

UCLA

Haoxiang Duan

UCLA

Wenxin Yang

Department of Materials Science and Engineering, University of California Los Angeles, Los Angeles, CA, 90095 USA

Yiushun Tong

UCLA

Xinyang Tong

UCLA

Yingke Zhu

UCLA

Ming Gong

UCLA

Ran Zheng

UCLA

Yongzhen Wu

East China University of Science & Technology https://orcid.org/0000-0003-3000-403X

Wei Chen

Huazhong University of Science and Technology, Optics Valley Laboratory https://orcid.org/0000-0002-2418-9210

Liyuan Han

Shanghai Jiao Tong University https://orcid.org/0000-0001-9766-9015

Article

Keywords: perovskite solar cell, ion migration, electric field, p-type contact, ion blocking contact, operational stability

Posted Date: April 17th, 2026

DOI: https://doi.org/10.21203/rs.3.rs-9374433/v1

License: This work is licensed under a Creative Commons Attribution 4.0 International License. Read Full License

Additional Declarations: There is **NO** Competing Interest.

Abstract

Halide ion migration is one of the most critical bottlenecks preventing the commercial deployment of perovskite solar cells (PSCs). Current mainstream strategies, relying solely on material-level defect passivation or physical barriers, remain insufficient to prevent the accumulation and penetration of activated ions during long-term operation. Here, we propose a physical paradigm, the ion blocking contact (IBC), that significantly suppresses ion migration via interfacial built-in electric field engineering. By constructing a targeted p-type ion blocking contact at hole transport layer (HTL) side, the dual-functional contact generates an electric field to repel ion migration, and simultaneously acts as a physical barrier to further enhance ion blocking. We validate this conceptual design across both n-i-p and p-i-n device architectures by employing strategies tailored to their distinct processing compatibilities. This strategy enables independently certified power conversion efficiencies of 26.29% and 27.05% for n-i-p and p-i-n architectures, respectively. Crucially, both IBC devices exhibit superior operational stability under 85°C maximum power point tracking, with the n-i-p and p-i-n devices showing less than 3% and 2% efficiency loss after 1200 and 2160 hours, respectively.

Main text

The power conversion efficiency (PCE) of perovskite solar cells has exceeded 27%, which is comparable to that of silicon solar cells [1]. However, the operational stability of perovskite solar cells is currently reported to be only a few thousand hours [2-7], lagging far behind that of silicon solar cells and failing to meet the requirements for commercial applications. The difference between perovskite materials and silicon materials lies in that: Silicon is held together by strong covalent bonds, which make the crystal structure rigid and stable, and thus ion migration is almost nonexistent; Hybrid organic-inorganic perovskite has a softer lattice due to weaker ionic and hydrogen bonds, which allows ions such as iodide ions to hop more easily between lattice site, especially under electric field, illumination, or heat stress [8-10]. Ion migration can result in compositional inhomogeneity and phase segregation [11-13]. Worse still, when migrating ions, especially iodide ions, diffuse out of perovskite towards interface, hole transport layer (HTL)/electron transport layer (ETL) or electrode, it will cause chemical reactions and result in interface deterioration, transport layer failure and electrode corrosion [10,14-16]. Therefore, confining ions inside perovskite materials is a prerequisite for realizing stable perovskite solar cells.

To effectively suppress ion migration, interfacial engineering has garnered extensive attention, encompassing strategies such as passivation layer [17,18], barrier layer [19,20], layered 2D perovskites [21-26], and so on. Admittedly, these interfacial layers mitigate ion migration via chemical passivation or physical blocking, boosting initial efficiencies and delaying early-stage device degradation. However, conventional interfacial strategies are inherently static. Driven by the continuous coupling of illumination, thermal stress, and operational electric fields during long-term operation, it is difficult for these ultrathin layers to provide a sufficient barrier against the chronic migration and accumulation of activated ions. Therefore,

relying solely on material-level defect modification or physical blocking is inadequate to resolve the ion migration dilemma during operation.

Here, we propose a physical paradigm, ion blocking contact (IBC), designed to suppress ion migration via active interfacial electric field engineering. Given that the built-in electric field in photovoltaic devices intrinsically directs from the electron transport layer (ETL) to the hole transport layer (HTL), we precisely construct a targeted p-type contact at the HTL/perovskite interface to induce a localized built-in electric field. This internal electric field acts as an active defensive shield, exerting a powerful electric repulsion against halide anions diffusing toward the HTL side. Moreover, the p-type contact itself is a physical barrier, thereby this dual-protection strategy significantly suppresses cross-interfacial ion migration.

To establish the universality of this physical paradigm and overcome the process blind spots inherent to specific device architectures, we conducted a coherent dual validation across both n-i-p and p-i-n configurations. Tailored to the distinct processing compatibilities of different interfaces, we employed divergent yet physically convergent engineering approaches: at the solution-processable top interface of the n-i-p architecture, we constructed a uniform, phase-pure 2D perovskite layer; conversely, at the highly solvent-sensitive buried interface of the p-i-n architecture, we introduced a hydrolyzed (3-aminopropyl) triethoxysilane (HAPTES)-modified alumina layer featuring terminal functional groups. Although these two strategies differ in material attributes and processing routes, physical characterizations confirm that they successfully create a built-in electric field in the perovskite bulk, thus significantly suppressing ion migration. Based on this mechanism, n-i-p and p-i-n devices both achieved independent third-party certifications, delivering top-tier power conversion efficiencies of 26.29% and 27.05%, respectively. Crucially, both IBC devices exhibit superior operational stability under maximum power point (MPP) tracking. Operating continuously at 85°C, the n-i-p and p-i-n devices showed negligible efficiency degradations of less than 3% after 1200 hours and less than 2% after 2160 hours, respectively. This work establishes the interfacial built-in electric field as the significant defense against ion migration.

Mechanism and construction of ion blocking contact

In conventional device architecture, the built-in electric field is predominantly located at the heterointerface between the perovskite and the transport layers. Consequently, when halide ions migrate to this interface, they inevitably diffuse into the transport layers driven by a substantial concentration gradient, despite the opposing electric field directed from the ETL to the HTL (Fig. 1a). To address this, we engineered a p-type contact on the HTL side to establish an internal electric field within the perovskite bulk. As halide ions approach this contact, they encounter a strong electric repulsion and are driven back into the perovskite interior, effectively preventing them from reaching the heterointerface and transport layers. More importantly, beyond this electric shielding, the p-type contact intrinsically acts as a robust physical barrier against ion migration. As depicted in Fig. 1b, this dual-protection mechanism ensures that halide ions are strictly confined within the perovskite, thereby significantly improving the overall device stability.

To construct the IBC structure in n-i-p solar cell, we deposited the alkylamine ligand solution on the wet perovskite precursor film before post annealing. In this experiment, we used hexan-1-amine hydroiodide. Then, the alkylamine ligand salts gradually penetrated inside the perovskite precursor film. According to our previous research work [27], we used mixed solvents to control the penetration depth. Finally, the perovskite precursor films with alkylamine ligand were placed on a hotplate for annealing. The schematic diagram is shown in Supplementary Fig. 1. As a result, a co-grown 2D (C2D) layer was formed on a crystallized 3D perovskite film, which enabled the formation of ion blocking contact. We used X-ray diffraction (XRD) to characterize the formation of the 2D material on the 3D perovskite. For pure 3D perovskite (hereafter named as pristine sample), the dominant XRD peaks belong to (001) and (002) crystal plane as shown in Fig. 1c. For IBC structure, the layer number of 2D perovskite is determined by the amount of organic spacer. After we precisely optimized the concentration of alkylamine ligand, the pure phase 2D perovskite with n value of 1, 2, 3 and 4 was achieved, corresponding to the ligand concentration of 8, 5, 3, and 2 mg/ml, respectively (Fig. 1c). For comparison, when alkylamine ligand was deposited on the annealed perovskite film as traditional passivation method (hereafter named as control sample), 2D perovskite with different n values can be observed (Supplementary Fig. 2), which is consistent with the previous research and can be mainly ascribed to the uneven lead iodide distribution and the organic spacer deposition [24,28]. Photoluminescence (PL) spectroscopy was further utilized to confirm the IBC structure. Except for the dominant peak for 3D perovskite material at around 810 nm, other peaks at 527 nm, 567 nm, 613 nm, and 656 nm can also be clearly observed, which corresponds to the 2D perovskite with different layer number (Supplementary Fig. 3). For control sample, the result is consistent with the XRD results, in which 2D layer with n=1 and 2 can be observed (Supplementary Fig. 4). Scanning electron microscope (SEM) was used to characterize the surface and cross-sectional morphology of IBC structure. It is observed that there were fewer lead iodide on the surface of control and IBC sample than on the pristine sample, resulting from the formation of 2D layer (Supplementary Fig. 5). From cross section view, we can observe 3D layer was covered by a thin 2D layer, and the crystallinity of 3D perovskite was almost the same (Fig. 1d). This implies that the incorporation of the 2D layer has negligible impact on the crystallinity of the underlying 3D perovskite, which can also be observed in XRD results in Fig. 1c.

To construct the IBC structure in p-i-n solar cell, We developed a HAPTES-functionalized alumina layer. For clarity, we term it a buried ion blocking contact (BIBC), as it is situated at the buried interface. To achieve this, the alumina surface was first hydroxylated to provide abundant grafting sites, followed by the subsequent grafting of HAPTES onto the alumina. Detailed procedures are provided in Supplementary Note 1. As shown in Fig. 1e,f, the emergence of a Si 2p signal in the ~102 eV region, together with a pronounced increase in the N 1s peak intensity at ~400 eV, provides direct evidence for the presence of HAPTES on the alumina surface. A concomitant shift in the Al-related features further indicates modification of the local coordination environment (Fig. 1g). The Al 2p peak first shifts toward higher binding energy due to the formation of electronegative Al-OH bonds, then slightly retreats as these groups are consumed to form Al-O-Si linkages during HAPTES grafting. To further verify the stable bonding between HAPTES and alumina, we monitored the variations in the surface contact potential

difference (CPD) via Kelvin probe force microscopy (KPFM) and the elemental compositions via X-ray photoelectron spectroscopy (XPS) following polar solvent washing and photothermal aging. We revealed that the BIBC remains chemically and electronically stable under both highly polar solvent exposure and elevated-temperature photo-thermal aging, which is a critical prerequisite for realizing highly efficient and durable perovskite solar cells. Detailed descriptions are provided in Supplementary Note 4. Considering the stability of the aforementioned samples under polar solvents and photo-thermal aging conditions, we will focus our subsequent studies on the ITO/PTAA, ITO/PTAA/alumina, and ITO/PTAA/BIBC substrates. Hereafter, untreated samples are denoted as pristine, samples with alumina as control, and samples incorporating the buried ion blocking contact as BIBC. Subsequently, perovskite films were deposited on ITO/PTAA, ITO/PTAA/alumina, and ITO/PTAA/BIBC substrates. XRD, UV-vis absorption spectroscopy, and top-view SEM revealed no discernible differences in crystallinity, optical absorption, or surface morphology among these samples (Supplementary Figs. 15-17), indicating that the introduction of alumina or BIBC interlayer does not perturb perovskite film formation. Cross-sectional SEM images further confirm the presence of the BIBC at the bottom interface, clearly resolving the interfacial layer between the electrode and the perovskite absorber (Fig. 1h).

Band alignment between ion blocking contact and perovskite film

Energy level alignment is one of the necessary preconditions for achieving efficient carrier extraction and transport in perovskite solar cells. In n-i-p device, we utilized ultraviolet photoelectron spectroscopy (UPS) to obtain the work function and the valance band maximum (VBM) of the C2D layer (Supplementary Fig. 18). Based on the band gap obtained from the tauc plot (Supplementary Fig. 19), we can deduce the energy level diagram for IBC structure with different n values (Fig. 2a). When n=1 or 2, the 2D layer showed a type I alignment with 3D perovskite material, which could be a barrier for charge extraction. While n=3, we can observe a near-perfect type II band alignment between the 2D layer and 3D material, showing the potential for effectively transporting holes and blocking electrons. More importantly, we observed that the pristine 3D perovskite film exhibits distinct n-type characteristics, which can likely be attributed to the low formation energy of n-type defects such as iodine vacancies or undercoordinated Pb ions. In contrast, the top 2D perovskite layer displays a p-type nature, presumably due to the preferred formation of shallow acceptor defects (e.g., Pb vacancy) induced by the bulky organic cations. Such an energy-level difference naturally facilitates the formation of a built-in electric field at the 2D/3D heterointerface. This internal field is highly advantageous: it not only provides a strong driving force for efficient charge carrier extraction, but also effectively suppresses the detrimental interdiffusion of iodide ions and bulky cations between the 3D and 2D perovskite layers, thereby substantially enhancing the structural stability. KPFM was further conducted to compare the contact potential difference for C2D layer with different n values (Fig. 2b). Deeper work function was observed when n value decreased from 4 to 1, which is consistent with the UPS results. For comparison, we also fabricated a sample with 2D layer via traditional method. The surface KPFM image is not as uniform as that with IBC structure, mainly due to the mixed 2D phase in control sample, which is shown in the XRD and PL results. In addition, from the atomic force microscope (AFM) results in Supplementary Fig. 20, the roughness was slightly reduced in IBC structure, which can be ascribed to the uniform growth of the

2D structure on top of the 3D perovskite film. Such a smoother interface in the IBC structure is highly beneficial for establishing intimate contact with the subsequent charge transport layer.

In p-i-n device, the formation of the ion blocking contact can be mainly attributed to the interaction between the perovskite material and HAPTES-modified alumina. Specifically, XPS reveals systematic binding-energy shifts of the perovskite core levels (Supplementary Fig. 21), accompanied by pronounced changes in surface potential as measured by KPFM (Fig. 2d). The detailed description has been summarized in Supplementary Note 5. Consistently, UPS measurements show distinct modifications of the perovskite surface energy levels (Supplementary Fig. 22 and Fig. 2c). The sequential downward shift of the Fermi level and the simultaneous upward movement of the valence band maximum lead to a narrowed gap between them, indicating a pronounced p-type shift at the perovskite surface. The pronounced p-type shift comes from the selective passivation characteristic primarily targeting electron-type defects. Electron-only (ITO/SnO_2/Perovskite/PCBM/Ag) and hole-only (ITO/PTAA/Perovskite/Spiro/Ag) devices incorporating the alumina or BIBC at the buried interface were fabricated. Using the space-charge-limited current (SCLC) method, we quantified the trap densities for both pristine and modified films. As shown in Fig. 2e,f, the results exhibit a distinct contrast: the electron trap density decreases significantly after modification, whereas the hole trap density shows negligible variation. The SCLC results provide quantitative physical evidence for the evolution of interfacial electronic states. For electron-only devices, the trap-filled limit voltage exhibits a distinct gradient decrease upon modification, which directly reflects a significant reduction in electron trap density. This observation aligns precisely with the Lewis base electron-donating effect revealed by XPS, where the alumina and BIBC layers act as electron donors to neutralize electron trap states associated with under-coordinated lead sites. In contrast, the trap-filled limit voltage for hole-only devices remains nearly constant, indicating that the modification system possesses a selective passivation characteristic primarily targeting electron-type defects, which manifests as a p-type shift of the Fermi level in KPFM and UPS measurements. Consequently, the reduction in electron traps confirmed by SCLC and the energy level reconfiguration revealed by UPS and KPFM constitute a synergistic mechanism. While the pristine perovskite typically exhibits n-type behavior due to a high density of electron-donating defects, the introduction of BIBC leads to a dramatic reduction in electron trap density, while the hole trap density remains nearly constant. By specifically neutralizing these n-type localized states, the BIBC effectively shifts the chemical potential toward the valence band, inducing a transition from n-type toward p-type characteristics at the interface [29,30]. Consequently, the perovskite in BIBC regions can be effectively doped.

Carrier dynamics for IBC/BIBC structure

Owing to the excellent band alignment, carrier extraction is expected to be more efficient for IBC and BIBC structure. For IBC sample, higher PL peaks were observed at wavelength around 810 nm in Supplementary Fig. 3, indicating less nonradiative recombination. Time-resolved photoluminescence (TRPL) was used to quantitatively analyze the carrier lifetime in perovskite materials (Supplementary Fig. 23). For pure 3D perovskite material without any post treatment, the lifetime is 1.16 μs, and it increased

to 1.50 μs in control sample. With IBC structure, the carrier lifetime is 2.31, 2.45, 2.59 and 2.35 μs with n=1, 2, 3 and 4, respectively, indicating the nonradiative recombination was greatly inhibited. We also test the TRPL spectra for IBC structure with HTL. The TRPL signals decayed faster for IBC structure with n=3, indicating faster hole transfer rate into the HTL due to the near-perfect energy level alignment (Supplementary Fig. 24). PL mapping test was also conducted to confirm the less nonradiative recombination and uniformity of IBC structure (Supplementary Fig. 25), from which we can observe that IBC structure with n=3 showed the higher photoluminescence intensity. For BIBC structure, this improvement in carrier dynamics was also corroborated by PL and TRPL measurements (Supplementary Figs. 26-27), which revealed reduced non-radiative recombination and enhanced carrier extraction. Electrochemical impedance spectroscopy (EIS) further elucidates the charge recombination kinetics at the interface (Supplementary Fig. 28). As shown in the Nyquist plots, the semicircle radius, which represents the recombination resistance (Rrec), increases dramatically from the pristine to the BIBC-modified samples. This substantial enhancement in Rrec signifies that the non-radiative recombination is effectively suppressed, directly supporting the SCLC results where a lower electron trap density was observed. The Mott-Schottky analysis further confirmed the enhanced charge-extraction driving force at the interface (Supplementary Fig. 29). The built-in potential (V_{bi}), derived from the x-intercept of the C^{-2}-V plots, increases from 1.18 V (Pristine) to 1.27 V (BIBC). This elevation in V_{bi} is a direct consequence of the optimized energy-level alignment, as previously indicated by UPS and KPFM. A higher V_{bi} facilitates more efficient separation of photogenerated carriers, which effectively suppresses interfacial recombination. This physical enhancement is highly consistent with the EIS results.

Photovoltaic performance of the device

Consequently, the introduction of IBC and BIBC fundamentally reconstructed the interfacial energetics and translated into pronounced photovoltaic enhancement. we fabricated perovskite solar cells with FTO/SnO_2/perovskite/2D or C2D/PTAA or spiro-OMeTAD/electrode structure and ITO/SAM or PTAA/alumina or BIBC/ perovskite/passivation/PCBM/BCP/electrode structure (Fig. 2g,j). Both IBC and BIBC methods played a positive role in improving power conversion efficiency. In PTAA-based devices, incorporation of IBC in n-i-p device increased the champion power conversion efficiency (PCE) from 23.05% to 25.24%, while incorporation of BIBC in p-i-n device increased the champion PCE from 24.51% to 26.00% (Fig. 2h,k, Supplementary Fig. 30 and Supplementary Tables 3-4). The integrated current density derived from the external quantum efficiency (EQE) spectra closely matched the J-V result, confirming the reliability of the photovoltaic metrics (Fig. 2i,l). More importantly, we observed higher EQE at wavelength at around 700-800 nm for n-i-p device and 400-500 nm for p-i-n device, resulting from better carrier extraction at IBC/HTL and BIBC/HTL interface. When replacing the PTAA layer by spiro-OMeTAD layer for n-i-p device and SAM layer for p-i-n device, the PCE boosted over 26% and 27%, respectively (Supplementary Figs. 31-32 and Supplementary Tables 5-6), which is among the top tier PCE for both n-i-p and p-i-n structure perovskite solar cells [5,31-35]. To further validate our results, an independent third-party institution certified the devices with a power conversion efficiency of 26.29% for n-i-p device and 27.05% (a steady-state efficiency of 26.87%) for p-i-n device (Supplementary Figs. 33-

35). The third-party certified power conversion efficiency shows excellent agreement with our laboratory-tested results, thereby validating the accuracy and reliability of our device evaluation. The steady state output and efficiency distribution were summarized in Supplementary Figs. 36-37. During the continuous tracking, the device performance exhibited negligible degradation, demonstrating its excellent operational reliability. Moreover, the narrow distribution of photovoltaic parameters confirms the high reproducibility of the IBC and BIBC strategy (Supplementary Figs. 38-39). To evaluate the scalability, we also fabricated 1 cm^2 standard cell, and the J-V curve and specific parameter were shown in Supplementary Figs. 40-41 and Supplementary Tables 7-8. The minimal PCE gap successfully demonstrates the excellent scalability of the IBC and BIBC strategy.

Establishment of an internal electric field

To visualize the spatial distribution of the electric field, cross-sectional KPFM was employed to map variations in the depletion region, including both height and potential profile (Fig. 3a-d). For pristine sample, the depletion region is located at the heterointerface between the 3D perovskite and the charge transport layer, so as the electric field obtained by differentiating the potential curve (Supplementary Fig. 42). While for IBC/BIBC structure, according to the UPS results, the 3D perovskite shows n-type conductivity and the ion blocking contact shows p-type conductivity. Therefore, the depletion region was regulated to the interface between 3D perovskite and ion blocking contact, rather than the HTL heterointerface, as highlighted by the red dashed circles. We also tested the location of the depletion region for control sample via cross section KPFM. The depletion region for control samples is still near the HTL heterointerface, similar to that of the pristine sample. This observation indicates that the depletion region in IBC/BIBC-modified devices extends into the perovskite bulk rather than being confined to the heterointerface, inducing an internal electric field inside the perovskite bulk. This induced internal electric field is expected to effectively suppress ion migration. Distinct from conventional passive passivation or blocking layers, this induced internal field serves as an active force to suppress ion migration. Typically, once mobile ions reach the heterointerface, their diffusion becomes inevitable due to the steep concentration gradient. However, the IBC/BIBC-induced electric field exerts an opposing electrostatic force that prevents iodide ions from approaching the heterointerface, thereby mitigating the onset of diffusion at its source (Fig. 3e,f). Meanwhile, for n-i-p device, the electric field also prevented the bulky cations migrating from C2D material to 3D material. This mechanism represents a paradigm shift from passive structural blocking to active field-assisted containment, which is a conceptually novel approach where the internal field acts as a repulsive wall.

Influence of IBC/BIBC on suppressing ion migration

To characterize the ability of IBC/BIBC structure on inhibiting ion migration, time of flight secondary ion mass spectrometry (TOF-SIMS) was used to characterize the ion migration in perovskite solar cells (Fig. 3g,k). After aging under MPP condition and 85 ℃, a large amount of iodide ions can be found inside the HTL in pristine sample, indicating that the iodide ion migrated across the heterointerface then inside the HTL. In control sample, the situation has somewhat improved, but there was still large amount of iodide

ions in HTL. For comparison, few iodide ions can be observed in the HTL of IBC/BIBC device after aging at 85 ℃, meaning that the iodide ions have been constrained inside the 3D perovskite material via the ion blocking contact. We also conducted the XPS on the HTL of aged pristine sample, control sample and IBC/BIBC sample in Fig. 3h,l, and the results were similar to that of TOF-SIMS, that is, few iodide signals can be observed in HTL of aged IBC/BIBC sample, and it is the opposite side in pristine and control sample. This phenomenon in the control sample can be primarily ascribed to the fact that the inhomogeneous, impure 2D layer and the alumina itself fail to establish a robust barrier to suppress ion migration. The XPS spectra of carbon elements for calibration is shown in Supplementary Fig. 43. The chemical invasion of iodide ions profoundly alters the semiconducting properties of HTL. UPS measurements reveal that for the pristine and control samples, the energy offset between the Fermi level and the valence band maximum in the aged PTAA layer is significantly larger than that of the fresh samples (Fig. 3i,m and Supplementary Figs. 44-45). This indicates a progressive loss of the p-type characteristic in PTAA as a direct consequence of iodide intrusion. Such electronic degradation hampers carrier extraction and ultimately deteriorates photovoltaic performance. Conversely, the PTAA in IBC/BIBC devices successfully maintains its robust p-type nature, ensuring efficient charge transport even after prolonged aging. Finally, the quantification of ion migration activation energy (Ea) as shown in Fig. 3j,n provides definitive kinetic evidence for this stabilization. The activation energy calculated from the Arrhenius plots of the conductivity is 0.39, 0.47, and 0.61 eV for pristine sample, control sample and IBC sample, and 0.43, 0.52, and 0.66 eV for pristine sample, control sample and BIBC sample. This elevated energy barrier quantitatively confirms that the IBC/BIBC-induced field-assisted containment effectively immobilizes mobile ions, thereby preserving the long-term operational stability of the device.

Stability of perovskite film with IBC/BIBC structure

After understanding the changes in HTL before and after aging, we also noticed the changes in the perovskite layer. For n-i-p device, we used chlorobenzene to wash the HTL away and then conducted XRD test on the aged perovskite film (Fig. 4a). There was almost no change for the IBC sample, which means that the C2D structure was stable and still played an important role in inhibiting ion migration. While in control sample, the 2D peak of n=2 almost disappeared, and the 2D peak of n=1 obviously weakened, thus the iodide ion can enter the HTL more easily than fresh sample. Via PL spectroscopy tests in Fig. 4b, we also found that 2D structure in the control sample severely collapsed after illumination aging under 85 ℃, losing the passivation effect and important role in blocking ion migration. For p-i-n device, SEM was employed to examine the peeled bottom surfaces of the perovskite films after aging to visually evaluate the structural preservation of the buried interface following the suppression of ion migration (Fig. 4c). For the pristine and control samples, the exposed buried interfaces exhibited a high density of pinholes. These morphological defects are attributed to localized lattice degradation triggered by ion migration, which accelerates the decomposition of the perovskite at the heterointerface. In contrast, the BIBC samples showed an almost intact interface with negligible pinholes, indicating that ion migration was effectively inhibited, and the structural integrity of the perovskite was successfully maintained.

Furthermore, in-situ biasing photoluminescence mapping provided a more direct visualization of the efficacy of the IBC/BIBC in suppressing ion migration (Fig. 4d,e). The experimental configuration for biasing and testing is illustrated in Supplementary Fig. 46, where a constant vertical bias of 1 V was applied. Under the influence of the external electric field, mobile ions are expected to migrate rapidly, thereby accelerating stoichiometric segregation and defect formation within the perovskite film. This degradation is manifested as a significant quenching of the PL intensity over time. It was clearly observed that the PL intensity of the pristine and control samples progressively decayed during the biasing period. Conversely, the PL intensity of the IBC/BIBC sample remained nearly constant. This result provides compelling evidence that the IBC/BIBC-induced internal electric field effectively counteracts ion migration, thereby preserving the optoelectronic quality of the perovskite under operational stress.

Operational stability of perovskite solar cells

International Summit on Organic Photovoltaic Stability (ISOS) protocols were used for operational stability test of the resulting IBC perovskite solar cells [36]. Attributed to the excellent ability of blocking ion migration for IBC/BIBC structure, when aged under continuous illumination and 85 ℃ under maximum power point (MPP) operating conditions, the n-i-p device still maintained over 97% of the initial PCE after 1200 hours, and the p-i-n device still maintained over 98% of the initial PCE after 2160 hours (Fig. 4f,g). By leveraging a robust built-in electric field, the IBC structure successfully blocks the interdiffusion of iodide ions and bulky cations between the 2D and 3D perovskite layers, and the BIBC structure successfully blocks the diffusion of iodide ions to HTL, thereby preserving the structural integrity of the heterojunction. Simultaneously, the robust ion blocking contact itself acts as a formidable physical barrier against ion migration. It is precisely this dual-protection mechanism that endows the IBC/BIBC-based perovskite solar cells with such remarkable long-term stability.

Discussion

Herein, we propose a paradigm-shifting mechanism to suppress ion migration in perovskite solar cells. Unlike conventional approaches that depend on passive interface layers, our strategy constructs a p-type ion blocking contact directly within the perovskite bulk. This architecture induces an internal electric field, actively suppressing ion migration through electric forces rather than relying on passive physical blocking. Moreover, the p-type contact itself serves as a formidable physical barrier against ion migration. This dual-protection mechanism effectively ensures both the long-term structural integrity and operational stability of the devices. We have successfully implemented this strategy in both n-i-p and p-i-n configurations, proving its coherent operation within a unified design. Consequently, the target n-i-p and p-i-n devices demonstrated extraordinary robustness, retaining over 97% and 98% of their initial efficiency after 1200 and 2160 hours of continuous maximum power point tracking (MPPT) under 85°C, respectively. This work provides a fundamentally new conceptual framework for mitigating ion migration in perovskite photovoltaics.

Declarations

Acknowledgments: This work was supported by MoleculaX Inc.

Author contributions: Z.S. and Y.Y. conceived the idea. Z.S. designed the experiment, performed data analysis, and wrote the manuscript. Z.S. led the fabrication of the solar cells. Y.W., W.C. and L.H. helped with the device certification. H.D. helped with PL mapping and XRD test. W.Y. helped with UPS and XPS test. Y.T. helped with SEM test. Y.Z helped with KPFM test. X.T. helped with EIS and C-V test. M.G., R.Z., Y.W., W.C. and L.H. participated in the discussion about the feasibility of the experiment. All authors discussed the results and commented on the manuscript. Z.S. and Y.Y. revised the manuscript.

Competing interests: The authors declare no competing interests.

Data and materials availability: All data are available in the main text or the supplementary information

References

1. Green, M. A. et al. Solar Cell Efficiency Tables (Version 66). *Prog. Photovoltaics* **33**, 795-810 (2025).
2. You, S. et al. C60-based ionic salt electron shuttle for high-performance inverted perovskite solar modules. *Science* **388**, 964-968 (2025).
3. Zhao, K. et al. peri-Fused polyaromatic molecular contacts for perovskite solar cells. *Nature* **632**, 301-306 (2024).
4. Yang, Y. et al. Amidination of ligands for chemical and field-effect passivation stabilizes perovskite solar cells. *Science* **386**, 898-902 (2024).
5. Liu, S. W. et al. Buried interface molecular hybrid for inverted perovskite solar cells. *Nature* **632**, 536-542 (2024).
6. Lin, Y. H. et al. Bandgap-universal passivation enables stable perovskite solar cells with low photovoltage loss. *Science* **384**, 767-775 (2024).
7. Gao, D. P. et al. Long-term stability in perovskite solar cells through atomic layer deposition of tin oxide. *Science* **386**, 187-192 (2024).
8. Ren, X. X. et al. Mobile iodides capture for highly photolysis- and reverse-bias-stable perovskite solar cells. *Nat. Mater.* **23**, 810-817 (2024).
9. Zhao, Y. et al. Suppressing ion migration in metal halide perovskite via interstitial doping with a trace amount of multivalent cations. *Nat. Mater.* **21**, 1396-1402 (2022).
10. Wang, Y. et al. Stabilizing heterostructures of soft perovskite semiconductors. *Science* **365**, 687-691 (2019).
11. Xu, J. X. et al. Triple-halide wide-band gap perovskites with suppressed phase segregation for efficient tandems. *Science* **367**, 1097-1104 (2020).
12. Zheng, L. K. et al. Strain-induced rubidium incorporation into wide-bandgap perovskites reduces photovoltage loss. *Science* **388**, 88-95 (2025).

13. Bai, Y. et al. Initializing film homogeneity to retard phase segregation for stable perovskite solar cells. *Science* **378**, 747-754 (2022).
14. Wang, T. et al. Transporting holes stably under iodide invasion in efficient perovskite solar cells. *Science* **377**, 1227-1231 (2022).
15. Besleaga, C. et al. Iodine Migration and Degradation of Perovskite Solar Cells Enhanced by Metallic Electrodes. *J. Phys. Chem. Lett.* **7**, 5168-5175 (2016).
16. Zhao, Y. C. et al. Mobile-Ion-Induced Degradation of Organic Hole-Selective Layers in Perovskite Solar Cells. *J. Phys. Chem. C* **121**, 14517-14523 (2017).
17. Xing, Y. F. et al. Simultaneous Interfacial Defect Passivation and Free-Volume Reduction by Fluorinated Hole Transport Materials for High-Performance Perovskite Solar Cells. *Adv. Mater.*, e13884 (2025).
18. Gao, Z. Y. et al. Phase-stable wide-bandgap perovskites enabled by suppressed ion migration. *J. Energy Chem.* **96**, 120-128 (2024).
19. Zai, H. et al. Wafer-scale monolayer MoS_2 film integration for stable, efficient perovskite solar cells. *Science* **387**, 186-192 (2025).
20. Li, N. X. et al. Barrier reinforcement for enhanced perovskite solar cell stability under reverse bias. *Nat.Energy* **9**, 1264-1274 (2024).
21. Wang, Y. R. et al. Homogenized contact in all-perovskite tandems using tailored 2D perovskite. *Nature* **635**, 867-873 (2024).
22. Azmi, R. et al. Double-side 2D/3D heterojunctions for inverted perovskite solar cells. *Nature* **628**, 93-98 (2024).
23. Sidhik, S. et al. Deterministic fabrication of 3D/2D perovskite bilayer stacks for durable and efficient solar cells. *Science* **377**, 1425-1430 (2022).
24. Damp heat-stable perovskite solar cells with tailored-dimensionality 2D/3D heterojunctions. *Science* **376**, 73-77 (2022).
25. Luo, L. et al. Stabilization of 3D/2D perovskite heterostructures via inhibition of ion diffusion by cross-linked polymers for solar cells with improved performance. *Nat.Energy* **8**, 294-303 (2023).
26. Tian, Y. et al. High-entropy hybrid perovskites with disordered organic moieties for perovskite solar cells. *Nat. Photonics* **18**, 960-966 (2024).
27. Shen, Z. et al. Efficient and stable perovskite solar cells with regulated depletion region. *Nat. Photonics* **18**, 450-457 (2024).
28. Tan, S. et al. Spontaneous formation of robust two-dimensional perovskite phases. *Science* **388**, 639-645 (2025).
29. Yin, W. J., Shi, T. T. & Yan, Y. F. Unusual defect physics in $CH_3NH_3PbI_3$ perovskite solar cell absorber. *Appl. Phys. Lett.* **104**, 063903 (2014).
30. Wang, Q. et al. Qualifying composition dependent p and n self-doping in $CH_3NH_3PbI_3$. *Appl. Phys. Lett.* **105**, 5 (2014).

31. Li, S. S. et al. High-efficiency and thermally stable $FACsPbI_3$ perovskite photovoltaics. *Nature* **635**, 82-88 (2024).
32. Park, J. et al. Controlled growth of perovskite layers with volatile alkylammonium chlorides. *Nature* **616**, 724-730 (2023).
33. Seo, G. et al. Efficient and luminescent perovskite solar cells using defect-suppressed SnO_2 via excess ligand strategy. *Nat.Energy* **10**, 774-784 (2025).
34. Lin, Y. X. et al. A $Nd@C_{82}$-polymer interface for efficient and stable perovskite solar cells. *Nature* **642**, 78-84 (2025).
35. Xiong, Z. et al. Homogenized chlorine distribution for >27% power conversion efficiency in perovskite solar cells. *Science* **390**, 638-642 (2025).
36. Khenkin, M. V. et al. Consensus statement for stability assessment and reporting for perovskite photovoltaics based on ISOS procedures. *Nat.Energy* **5**, 35-49 (2020).

Materials and Methods

Materials

TCO was purchased from Suzhou Sunyo Tech. $SnCl_2.2H_2O$, Thioglycolic acid (TGA), Urea, dimethyl formamide (DMF), dimethyl sulfoxide (DMSO), acetonitrile (ACN) chlorobenzene, chloroform, isopropyl alcohol, 4-tert-butylpyridine (tBP), lithium Bis(trifluoromethanesulfonyl)imide salt (Li-TFSI), ethanol, APTES and Cesium iodide (CsI) were purchased from Sigma-Aldrich. Alumina was purchased from US Research Nanomaterials, Inc. Lead iodide (PbI_2), Lead bromide ($PbBr_2$), Tris(Pentafluorophenyl)Borate (TPFB) and hexan-1-amine hydroiodide were purchased from Tokyo Chemical Industry. Formamidine hydroiodide (FAI), methylammonium iodide (MAI), methylamine hydrobromide (MABr) and methylamine hydrochloride (MACl) were purchased from Greatcell Solar Materials. 2,2',7,7'-Tetrakis [N,N-di (4-methoxyphenyl)amino]-9,9'-spirobifluorene (Spiro-OMeTAD), Poly[bis(4-phenyl)(2,4,6-trimethylphenyl)amine (PTAA), 4PADCB, EDADI, C_{60}, PCBM, and BCP were purchased from Xi'an Polymer Light Technology.

Perovskite solar cell fabrication

n-i-p device

The FTO substrate was cleaned through ultrasonic with detergent, deionized water, acetone, and IPA successively. After being cleaned and dried by air flow, the FTO glass was treated with ultraviolet plasma for 30 min. The SnO_2 layer was prepared via a chemical bath deposition method. The PbI_2 solution was prepared by dissolving 1.48 M PbI_2 into 1 ml DMF/DMSO mixed solvent (95:5/v:v). The solutions were stirred for at least 6 h before use. The FAI/MABr/MACl solution was prepared by dissolving 85 mg FAI, 4 mg MABr and 10 mg MACl in 1 ml IPA. The PbI_2 solution was spin-coated on the substrate at 1,500 r.p.m. for 30 s, and then the FAI/MABr/MACl solution spin-coated on the substrate at 1,500 r.p.m. for 30 s to

form the precursor film. For pristine sample, the sample was transferred to the hotplate for annealing at 150 °C for 15 min in ambient environment (the humidity is approximately 30%). For control sample, after annealing, the hexan-1-amine hydroiodide solution (3 mg/ml in CF/IPA=6/4) was sprayed on the perovskite film, and then annealed at 100 °C for 10 min. For IBC sample, before annealing, the hexan-1-amine hydroiodide solution (8, 5, 3, 2 mg/ml in CF/IPA=6/4) was sprayed on the perovskite precursor film, and then the sample was transferred to the hotplate for annealing at 150 °C for 15 min in ambient environment (the humidity is approximately 30%). The following preparation procedures of the HTL and electrode showed no difference for all devices: spiro-OMeTAD (75 mg ml^{-1} in CB) solution with 4-tert-butylpyridine and Li-TFSI doping or PTAA (30 mg ml^{-1} in CB) solution with 10 wt% TPFB doping was spin-coated at 3,000 r.p.m. as the HTL; finally, counter electrode was deposited via thermal evaporation.

p-i-n device

The ITO substrate was cleaned through ultrasonic with detergent, deionized water, acetone, and IPA successively. After being cleaned and dried by air flow, the ITO glass was treated with ultraviolet plasma for 20 min. The PTAA solution (2 mg/ml in CB) or 4PADCB solution (1 mg/ml in ethanol) was spin coated on the ITO substrate at 4000 rpm for 30 s, and then transferred to the hotplate for annealing at 100 °C for 10 min. For modified devices, the dispersion solution of alumina or HAPTES-modified alumina (2 mg/ml in IPA) was coated onto the substrate at 4000 rpm for 30 s, and then transferred to the hotplate for annealing at 100 °C for 10 min. The 1.6 M perovskite precursor solution was prepared with the composition $Cs_{0.05}(FA_{0.95}MA_{0.05})_{0.95}PbI_{2.85}Br_{0.15}$ containing 3% excess PbI_2 and 12% MACl. The precursors were dissolved in a mixed solvent of DMF and DMSO (4:1, v/v). The solution was then deposited onto substrates by spin coating. Specifically, 40 μL of the precursor solution was dispensed onto the substrate and spin-coated using a two-step program of 1000 rpm for 12 s followed by 5000 rpm for 38 s. During the second step, 300 μL of chlorobenzene was dropped onto the spinning substrate at 38 s as an antisolvent. The resulting films were subsequently annealed at 100 °C for 15 min to form the perovskite layer. An EDAI solution (1 mg mL^{-1} in IPA) was dynamically spin-coated onto the perovskite films at 5000 rpm for 30 s with a dispensing volume of 120 μL, followed by thermal annealing at 100 °C for 5 min. Subsequently, a PCBM solution (25 mg mL^{-1} in chlorobenzene) was deposited by spin coating at 2500 rpm for 30 s using 40 μL of solution. A BCP solution (1 mg mL^{-1} in IPA) was spin-coated at 5000 rpm for 30 s with a dispensing volume of 40 μL. Finally, 100 nm Ag was thermally evaporated as the top electrode under high vacuum to complete the device fabrication. For stability test, we used PTAA as HTL rather than 4PADCB. To replace PCBM and BCP layer, 30 nm C_{60} was thermally evaporated on the perovskite film, followed by 20 nm tin oxide layer made by atomic layer deposition (ALD). Finally, 100 nm Au was thermally evaporated as the top electrode under high vacuum.

Encapsulation

A designed glass was covered over the PSCs with UV-curable adhesive applied at the edges of the PSCs, followed by continuous long-wavelength UV curing for 7.5 min. The encapsulation was finished in a nitrogen glove box.

Characterization

The particle size distribution was measured by dynamic light scattering (DLS) using a Zetasizer Nano ZS. Contact angle was performed on VCA OPTIMA contact angle system. TGA was performed on PerkinElmer thermogravimetric analyzer TGA 8000. Electrochemical impedance spectroscopy (EIS) and Mott-Schottky (M-S) measurements were performed using a precision LCR meter (Hewlett Packard 4284A). XRD was performed on Panalytical powder X-ray diffractometer. SEM was performed on FEI Teneo scanning electron microscope. Steady-state PL was performed on cryogenic-temperature photoluminescence (Spectrometer: Acton SP2500). UV-vis absorption spectra were performed on U-4100 spectrophotometer (Hitachi) equipped with integrating sphere. XPS/UPS was performed on DLD Axis Ultra. A He dIBCharge lamp, emitting ultraviolet energy at 21.2 eV, was used for excitation. TRPL was performed on micro-photoluminescence spectroscopy (Spectrometer: Acton SP2500). AFM/KPFM was performed on Dimension Icon Scanning Probe Microscope (Bruker Nano, Inc.). PL mapping was performed on Confocal SP8 MP-DIVE-FLIM with Leica TCS-SP8-MP Deep In Vivo imaging system. *J-V* curves were tested by Keithley 2400 source measure unit under a simulated AM 1.5G spectrum, with a solar simulator (Enlitech, Taiwan), in ambient condition. The forward scan range is -0.1 V to 1.3 V, and the reverse scan range is 1.3 V to -0.1 V. The intensity calibration of the light was done by a National Renewable Energy Laboratory (NREL)-certified Si photodiode with a KG-5 filter. EQE test was performed on an integrated system QE-R3018 (Enlitech, Taiwan). TOF-SIMS was performed on the focused ion beam TOF-SIMS spectrometer (GAIA). Arrhenius plots of the conductivity were performed on the Lakeshore Cryogenic-Temperature Probe Station. Stability test was performed on Fluxim's Litos Lite, which enables high-throughput solar cell research with advanced JV, MPP and stability testing under ISOS protocols.

Figures

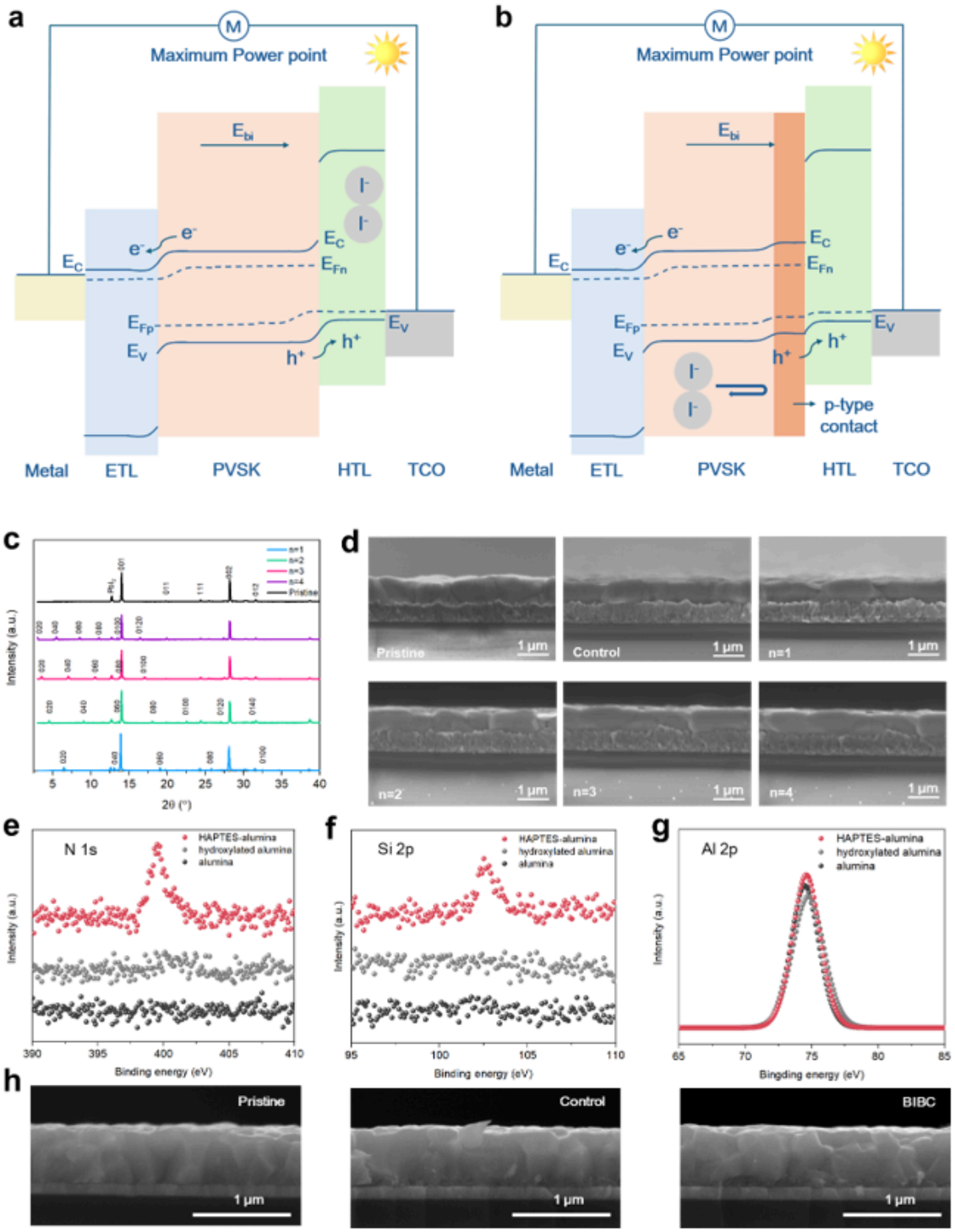


Figure 1

Formation of IBC/BIBC structure. a,b, Energy band diagrams of perovskite solar cells with (b) and without (a) the IBC structure under MPP condition. c, XRD results of pristine 3D perovskite film and IBC structure with different n values. d, Cross section SEM images of pristine 3D perovskite film wi/wo traditional passivation and IBC structure with different n values. The scale bar is 1 μm. e, XPS of the N 1s core level on alumina, hydroxylated alumina, and HAPTES-alumina. f, XPS of the Si 2p core level on

alumina, hydroxylated alumina, and HAPTES-alumina. g, XPS of the Al 2p core level on alumina, hydroxylated alumina, and HAPTES-alumina. h, Cross section SEM images of pristine sample (pure perovskite), control sample (with alumina) and BIBC sample (with HAPTES-alumina).

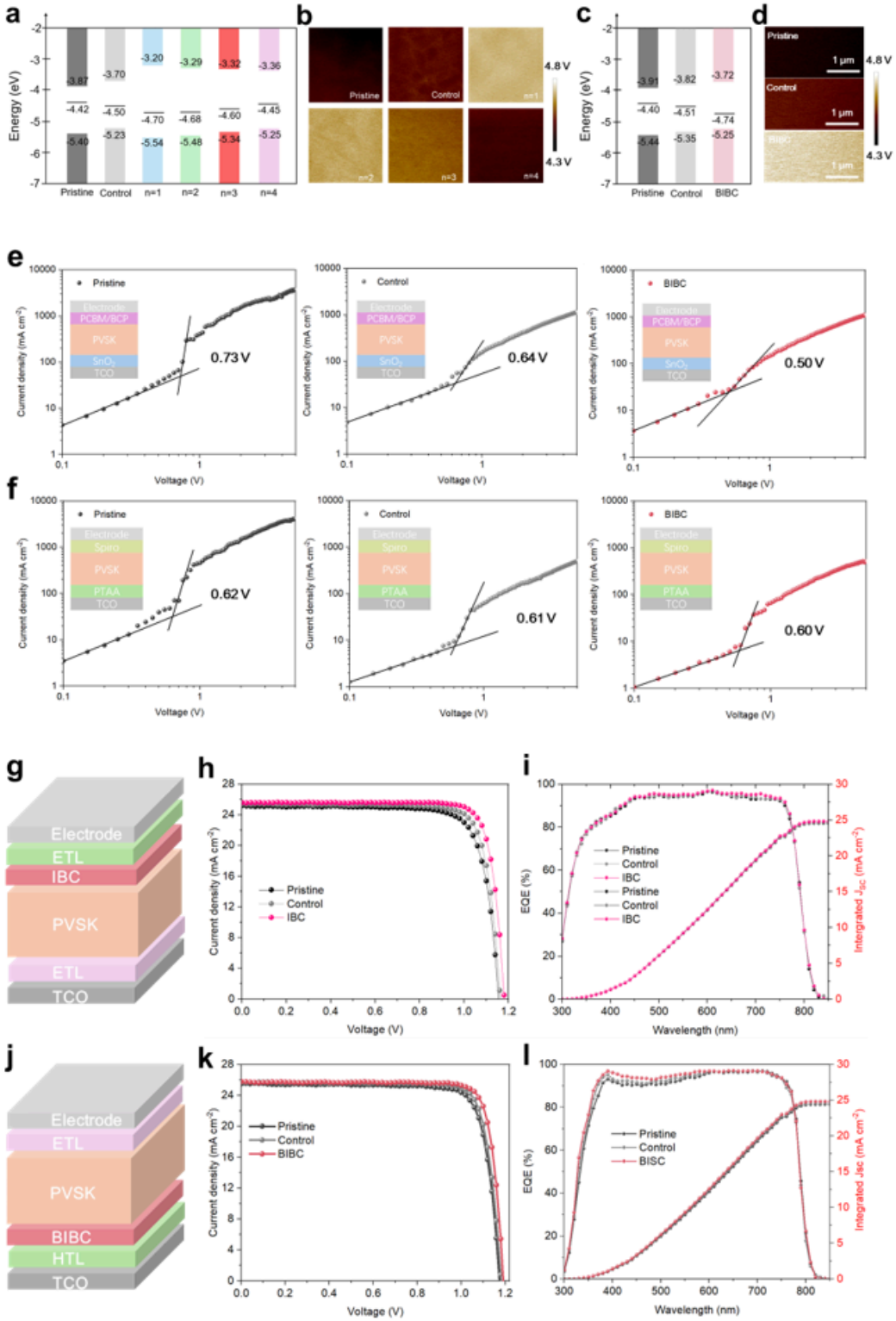


Figure 2

Energy level and device performance for IBC/BIBC structure. a, Energy level alignment for IBC structure with different n values and 3D perovskite. b, Surface KPFM images of IBC structure with different n values. The test area is 3 μm by 3 μm. c, Energy level alignment for pristine sample (pure perovskite), control sample (interact with alumina) and BIBC sample (interact with HAPTES-alumina). d, Surface potential measured by KPFM of pristine sample (pure perovskite), control sample (interact with alumina) and BIBC sample (interact with HAPTES-alumina). e, Space-charge-limited current measurement based on the electron-only geometry. f, Space-charge-limited current measurement based on the hole-only geometry. g, Configuration schematic of perovskite solar cell with IBC. h, *J-V* curves of pristine, control and IBC devices under 1 sun illumination with PTAA as HTL. i, External quantum efficiency curve of pristine, control and IBC devices over 300 to 850 nm wavelengths, and their corresponding integrated J_{SC}. j, Configuration schematic of perovskite solar cell with BIBC. k, *J-V* curves of pristine, control and BIBC devices under 1 sun illumination with PTAA as HTL. l, External quantum efficiency curve of pristine, control and BIBC devices over 300 to 850 nm wavelengths, and their corresponding integrated J_{SC}.

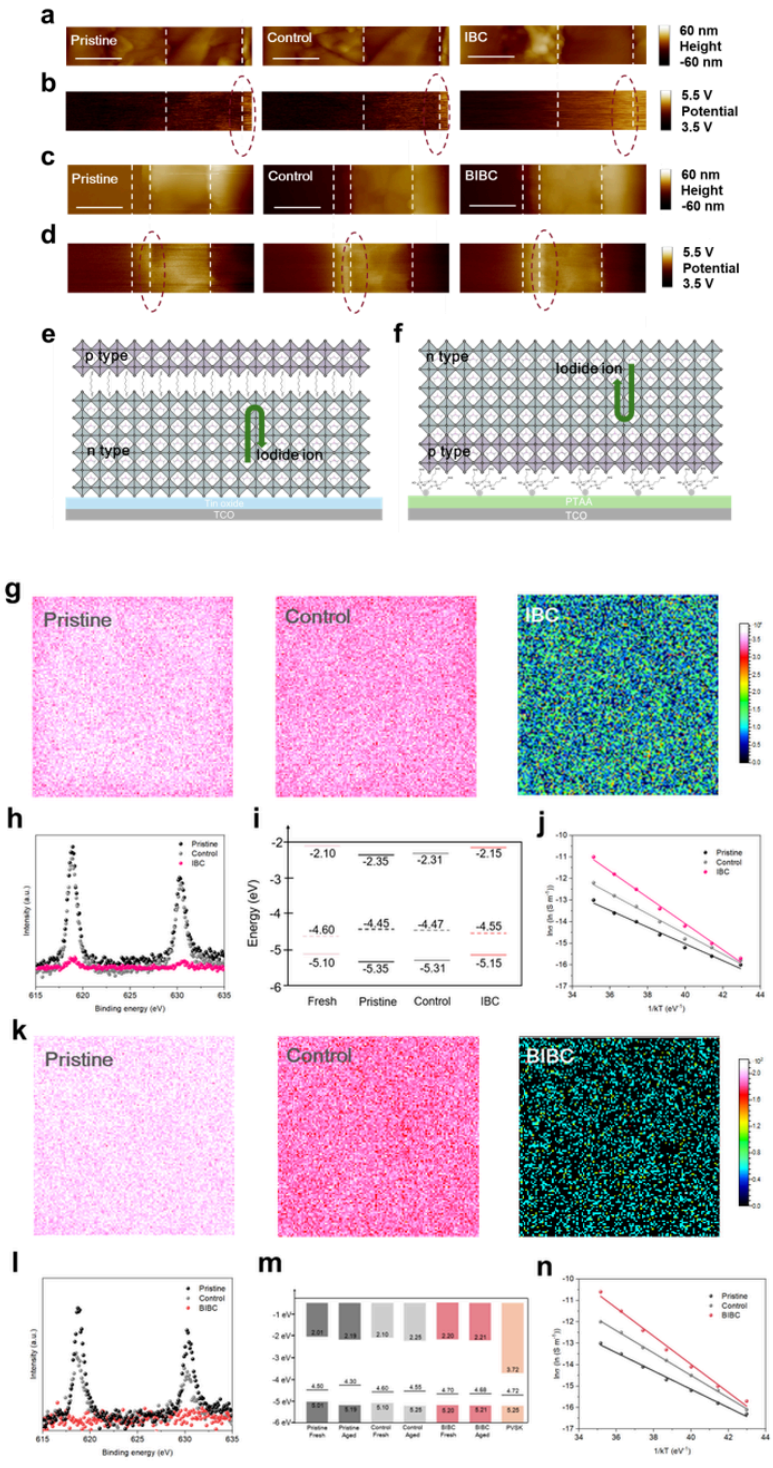


Figure 3

The formation of electrical field and the impact of IBC/BIBC on iodide ion migration. a,b, Cross section KPFM images of the pristine, control and the IBC device with n=3, including both height (a) and potential profile (b). The scale bar is 500 nm. c,d, Cross section KPFM images of the pristine, control and the BIBC device, including both height (c) and potential profile (d). The scale bar is 500 nm. e, f, Schematic diagrams illustrating the effect of the IBC/BIBC structure on suppressing iodide ion migration. g, Time of

flight secondary ion mass spectrometry on the HTL of the aged pristine, control and the IBC device with n=3. The test area is 100 μm by 100 μm. h, XPS results of iodide element signal for HTL of the pristine, control and the IBC device with n=3 after aging under MPP and 85 ℃ condition for 800, 800 and 1200 hours. i, Energy level evolution of PTAA HTL before and after aging under MPP and 85 ℃ condition for 800, 800, 1200 hours for the pristine, control and the IBC device with n=3. j, Arrhenius plots of the conductivity of the pristine sample, control sample and the IBC sample with n=3. k, Time of flight secondary ion mass spectrometry of iodide element signal on the HTL of the aged pristine, control and BIBC device. The devices were aged under MPPT and 85°C for 1000 hours. l, XPS results of iodide element signal for HTL of the aged pristine, control and BIBC device. The devices were aged under MPPT and 85°C for 1000 hours. m, Energy level evolution of PTAA HTL before and after aging for the pristine, control and BIBC device. The devices were aged under MPPT and 85°C for 1000 hours. n, Arrhenius plots of the conductivity of the pristine, control and BIBC device.

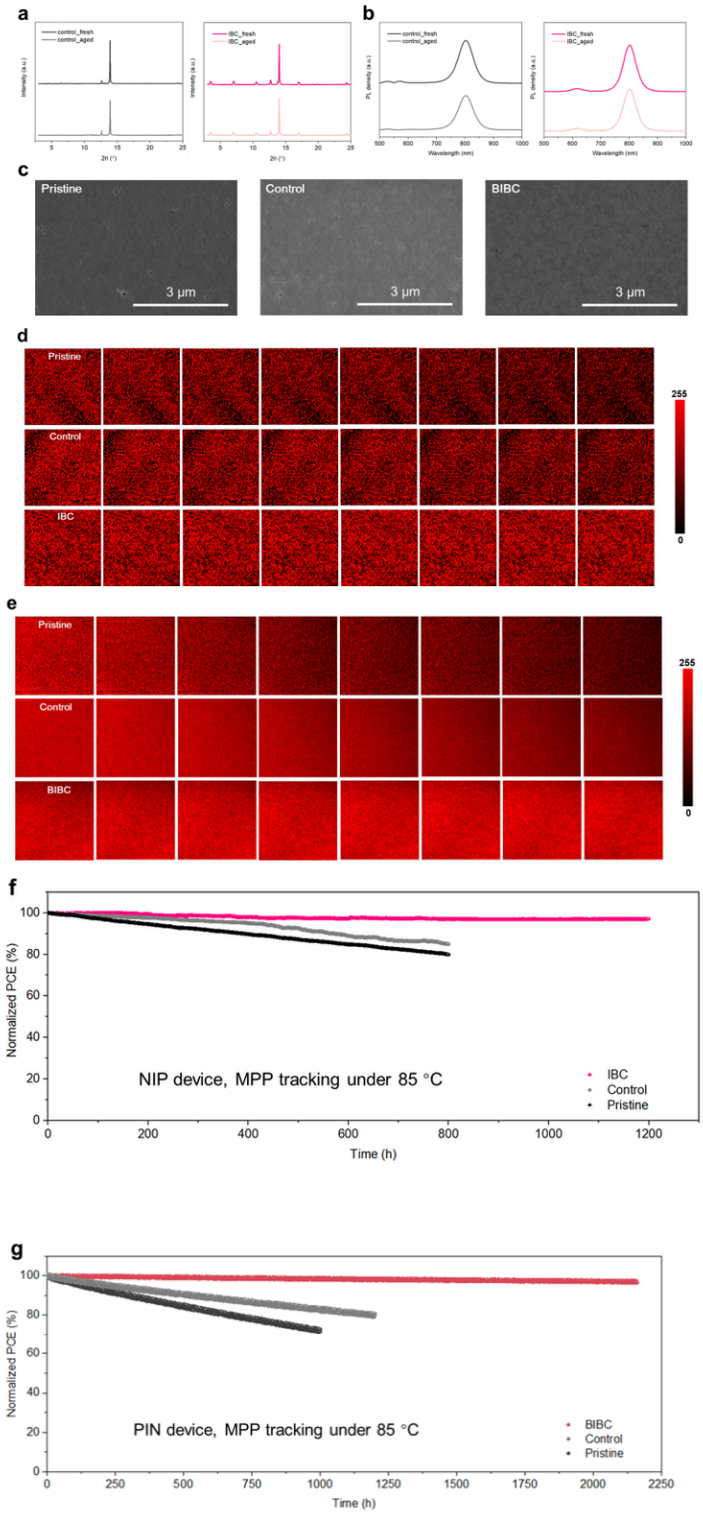


Figure 4

Characterization on the stability of perovskite films and devices. a, XRD patterns evolution of the control sample and the IBC with n=3 after aging under MPP and 85 ℃ condition for 800 and 1200 hours. b, Steady-state PL results evolution of the control sample and the IBC with n=3 after aging under MPP and 85 ℃ condition for 800 and 1200 hours. c, SEM image of the perovskite bottom interface for the pristine, control and BIBC device. The devices were aged under MPPT and 85°C for 1000 hours. d, PL

mapping results of the pristine, control and the IBC with n=3. The applied bias is 1 V, and the duration is 10 minutes. The test area is 100 μm by 100 μm. e,PL mapping results of the pristine, control and BIBC sample. The test area is 300 μm by 300 μm. f, Maximum power point tracking of encapsulated pristine, control, and IBC perovskite solar cells, measured at 85 °C under simulated AM 1.5G illumination, using PTAA as the hole transport layer. g, Maximum power point tracking of encapsulated pristine, control, and BIBC perovskite solar cells, measured at 85 °C under simulated AM 1.5G illumination, using PTAA as the hole transport layer.

Supplementary Files

This is a list of supplementary files associated with this preprint. Click to download.

- SupplementaryInformation.docx